# Mapping the Antarctic Grounding Zone from ICESat-2 Laser Altimetry

Tian Li[1], Geoffrey J. Dawson[1], Stephen J. Chuter[1], Jonathan L. Bamber[1]

[1]Bristol Glaciology Centre, School of Geographical Sciences, University of Bristol, Bristol, BS8 1SS, UK

5   *Correspondence to*: Tian Li (tian.li@bristol.ac.uk)

**Abstract.** We present the results of mapping the grounding zone of the Antarctic Ice Sheet using laser altimetry from the ICESat-2 satellite, based on a combination of repeat track data and crossover analysis of ascending and descending tracks. We use a new automated method to provide estimates for both the landward limit of ice flexure and the inshore limit of hydrostatic equilibrium by detecting the ocean tidal signals, and is demonstrated on the Larsen C Ice Shelf in the Antarctic

10   Peninsula. The results show a 2 times increase in number of observations of the grounding line location compared to ICESat-1, as well as improved precision. The mean absolute separation and the standard deviation between our ICESat-2 derived grounding line and DInSAR grounding line product are 0.29 km and 0.31 km, respectively. The beam pair structure of ICESat-2 enables us to derive the grounding zone features from a minimum of two repeat cycles. Our results demonstrate that ICESat-2 can provide high precision and density observations of grounding line in both space and time. This new

15   method can improve the efficiency of grounding zone calculation and can be applied to other regions of the Antarctic Ice Sheet.

## 1 Introduction

The accelerating mass loss of the Antarctic ice shelves can trigger increases in ice discharge from the grounded ice sheet through the grounding line (hereinafter referred to as GL) and therefore increase contribution to the global sea level rise

20   (Paolo et al. 2015). The GL is the point where the grounded ice sheet detaches from the bedrock and begins to float, and where the ice sheet is discharged into the ice shelves and the ocean. Ice discharge calculations are sensitive to the assumed location of the GL and therefore accurate GL location is required for the mass balance estimates of the grounded ice sheet (Chuter and Bamber 2015; Rignot et al. 2019). Changes in GL position are a key indicator of the Antarctica Ice Sheet mass imbalance (Schoof 2007). Rapid GL retreat of glaciers in the Amundsen Sea Sector between 1992 and 2011 observed from

25   ERS-1/2 satellite radar interferometry (Rignot et al. 2014), and the accelerating retreat of ~65% of the GL along the Bellingshausen Sea Sector between 1990 and 2015 from Landsat optical images (Christie et al. 2016) reflect an ocean-driven glacial mass loss in West Antarctica. Thus, accurate knowledge of the GL position and its changes are critical for multiple applications including ice sheet numerical modelling (Joughin et al. 2010), mass budget studies and assessing ice sheet stability.

30    The GL (point G in Figure 1) lies towards the landward edge of a transition zone between the fully grounded ice sheet (landward limit of tidal flexure shown as point F in Figure 1) and the freely-floating ice shelf (inshore limit of hydrostatic equilibrium shown as point H in Figure 1), forming the grounding zone (hereinafter referred to as GZ) (Fricker and Padman 2006). Its width depends on ice thickness and rheology as well as the combined effects of bed topography, tidal motion and the GL shape. The GL position is difficult to observe directly because it is at the bottom of the ice sheet. However, the

35    surface features of the GZ, such as the landward limit of tidal flexure of the ice surface (point F in Figure 1) which is the closest detectable surface feature to the true GL point G, mapped by satellite remote sensing techniques, can be used as a proxy for GL position.

The most accurate method, to date, for calculating the landward limit of ice flexure induced by tidal motion is using differential synthetic aperture radar interferometry (DInSAR) (Rignot et al. 2011). This method, however, is constrained by

40    the availability of suitable short temporal repeat pass SAR images, and there are relatively few regions where the method has been applied repeatedly (Friedl et al. 2019; Hogg et al. 2017). The flexural point F as well as the hydrostatic point H (Figure 1) has also been derived using repeat tracks of ICESat-1 laser altimetry data (Brunt et al. 2010; Fricker and Padman 2006) and from pseudo crossovers of CryoSat-2 radar altimetry data (Dawson and Bamber 2017). Both these methods can provide additional data for regions where the DInSAR derived GL information is unavailable. ICESat-1 repeat track analysis proved

45    to be a robust method for analysing the GZ, but its coverage and temporal resolution were limited due to the requirement of multiple repeat tracks from different campaigns (Brunt et al. 2010; Fricker and Padman 2006). In addition, the detection of GZ from ICESat-1 laser altimetry was based on visual interpretation which required a large amount of manual intervention (Brunt et al. 2010; Brunt et al. 2011; Fricker and Padman 2006).

The launch of ICESat-2 on 15 September 2018, as a successor to the ICESat-1 satellite mission, can achieve higher along-

50    track spatial resolution as well as nine times better coverage compared with its predecessor, providing the potential to map the GZ with greater accuracy and spatio-temporal coverage (Markus et al. 2017). ICESat-2 measures the ice sheet surface elevation at a repeat cycle of 91 days (Markus et al. 2017). The Advanced Topographic Laser Altimeter System (ATLAS) onboard ICESat-2 has three beam pairs in comparison with the single beam of the Geoscience Laser Altimeter System (GLAS) onboard ICESat-1. The across-track spacing between each beam pair is approximately 3.3 km with a pair spacing of

55    90 m. The along track sampling interval of each beam is 0.7 m with a nominal 17 m diameter footprint compared with the 170 m along-track spacing of ICESat-1 (Markus et al. 2017). In this study, we investigate the ability of using ICESat-2 data to map the Antarctic GZ and present a computationally efficient technique to measure the flexural point F and hydrostatic point H based on the repeat track data in combination with crossover data from ascending and descending tracks. We chose the Larsen C Ice Shelf in the Antarctic Peninsula to test this new methodology, as it is one of the northernmost ice shelves in

60    Antarctica with highest cross track spacing and the largest ice shelf in the Antarctic Peninsula with a range of different

surface slopes at the GZ (Jansen et al. 2010), it also experiences a large average tidal range of ~2 m, which facilitates testing the approach and proving its suitability for being applied to the whole of the Antarctica.

## 2 ICESat-2 Data

We used 12 months of the ICESat-2 Land Ice Along-Track Height Product ATL06 version 2 data spanning from October
65  2018 to November 2019 in this study. The ATL06 elevation measurements are derived from the individual photon elevation observations, averaged over a 40 m length segment. The segments overlap by 50% along each of the six ground tracks, thus the ATL06 elevation measurements are separated by 20 m along each ground track (Smith et al. 2019). Five cycles exist during the study period but only cycles 3, 4 and 5 are exact repeat cycles. Due to technical issues in the first two cycles, ICESat-2 did not point at the Reference Pair Track (RPT) which is the half-way between the predefined locations of two
70  ground tracks that make up a pair. Among all five cycles, three repeat cycles from March 29, 2019 to November 15, 2019 were used in a repeat track analysis for the GZ estimation, while data from all five cycles were used in a crossover analysis by using ascending and descending tracks.

The ATL06 elevation data have been corrected for ocean-loading tide, pole tide, and solid earth tide (Neumann et al. 2019). Since the method used in this study of estimating GZ features relies on detecting the vertical movements of floating ice due
75  to ocean tides, we did not add the correction for ocean tide and 're-tided' the ocean-loading tide (Fricker and Padman 2006). We used the ATL06_quality_summary flag to remove poor quality elevation measurements, which can be a result of clouds or random clustering of background photons (Smith et al. 2019). We also used the along-track slope parameter to perform a height consistency check between adjacent elevation measurements along each ground track. This was achieved by calculating the neighbouring elevations based on the along-track slope and comparing to the original surface elevations for
80  the two neighbouring measurements (Arendt et al. 2019). We only used data where the differences between the original elevations and the estimated elevations were lower than 2 m. In addition, the surface elevation was also compared with the reference DEM Reference Elevation Model of Antarctica (REMA) (Howat et al. 2019) provided in the ATL06 product. The elevation data were discarded if the elevation differences with REMA fell outside a ±150 m threshold. The ICESat-2 ATL06 elevation data from repeat cycles 3, 4 and 5 on the Larsen C Ice Shelf are shown in Figure 2.

85  ## 3 Methodology

### 3.1 Repeat track analysis

To measure the vertical motion of floating ice induced by ocean tides, we used a repeat track analysis similar to the approach used with ICESat-1 data by calculating the elevation anomalies for each repeat track (Brunt et al. 2010). However, now using the beam pairs of ICESat-2 we can also apply a cross-track slope correction in order to reduce noise caused by rough
90  terrain, which facilitated the automation of GZ mapping. The workflow of the repeat track analysis is shown in Figure 3. It

includes two parts: 1) the cross-track slope correction of surface elevation and the elevation anomaly calculation; 2) the GZ features estimation from the corrected elevation anomalies.

At the time of this study, only three exact repeat cycles were available. To maximise the number of repeat tracks to be used in the analysis, we treated two ground tracks that make up a pair from each repeat cycle as individual repeat tracks. This resulted in two repeat tracks per cycle for one beam pair and six repeat tracks for one beam pair from three repeat cycles (Figure 4a). The two ground tracks in a beam pair from one cycle are separated by ~90 m and the separation between same side ground tracks in a pair from different repeat cycles is less than 10 m. This is a marked improvement compared with ICESat-1 where the repeat track separation can exceed 100 m (Brunt et al. 2010). We used the average location of individual RPT from each repeat cycle for one beam pair as the nominal reference track to be used in the repeat track analysis, at an along-track interval of 20 m.

When using the automated repeat track analysis to estimate the GZ features, a reference GL estimate is needed (Figure 3). Here we used Depoorter et al. (2013) GL as it is the most complete grounding line product to date, compiled from all current available data. For the GZ calculation on ice rises and ice rumples, the MEaSUREs GL product was used (Mouginot 2017). The initial GL input was calculated as the intersection between the nominal reference track and the reference GL product. Only ATL06 elevation measurements within a window size of 12 km landward and seaward of the initial GL input along the nominal reference track were used. The grounding line of the Larsen C Ice Shelf was stable and therefore unlikely to have experienced rapid changes (Konrad et al. 2018), thus the choice of the above two reference GL products and the 24 km calculation window are suitable for the GZ calculation in this region. In order to improve calculation efficiency, data points with the elevation higher than 300 m were removed as the surface elevation of GZ is unlikely to exceed this threshold based on the hydrostatic equilibrium assumption. The ICESat-2 elevation measurements located in open water were also discarded by using the MEaSUREs Antarctic coastline mask (Mouginot 2017).

The elevation change calculated from repeat tracks is a combination of cross-track slope induced elevation change and temporal elevation changes such as snow accumulation or ablation, and vertical tidal displacement. As only 8 months of repeat cycles from March to November 2019 were used, temporal elevation changes due to snow accumulation or ablation were likely to be minimal and were disregarded in this study. Elevation change due to ocean tides is the only factor needs to be considered when estimating GZ, thus the elevation change caused by large cross-track slope in high sloping areas can make it difficult to extract the GZ features (Moholdt et al. 2010). Here we used the cross-track slope parameter $\frac{dh}{dy}$ shown in Figure 4a to correct the cross-track slope induced elevation changes and interpolated to the nominal reference track. We calculated the interpolated elevation $h_{LI,Ref}$ at the nominal reference track for the elevation of one ground track, $h_{LI,G}$ using the Eq. (1),

$$h_{LI,Ref} = h_{LI,G} - \frac{dh}{dy}(y_{ATC,G} - y_{ATC,Ref}) \tag{1}$$

where the cross-track slope $\frac{dh}{dy}$ for two ground tracks in a beam pair was calculated using the Eq. (2),

$$\frac{dh}{dy} = \frac{h_{LI,L} - h_{LI,R}}{y_{ATC,L} - y_{ATC,R}} \qquad (2)$$

$h_{LI,L}$, $h_{LI,R}$ are the elevations of left and right ground tracks that make up a beam pair. $y_{ATC,L}$, $y_{ATC,R}$ and $y_{ATC,Ref}$ are the y

125    coordinates measured perpendicular to the Reference Ground Track (RGT) for the left and right ground tracks, and the nominal reference track (Figure 4a), respectively. The average of all cross-track slope corrected elevations from each repeat track at the nominal reference track was taken as the reference elevation in GZ estimation. We also only used data where there were at least four repeat tracks..

After the cross-track slope correction for each ground track in a pair, a set of 'elevation anomalies' were estimated by

130    subtracting the reference elevation profile from the cross-track slope corrected elevation profiles of each individual repeat track, which are shown as the color-coded dot curves in Figure 5b. The elevation anomalies calculated from the original surface elevation without cross-track slope correction are shown in Figure 5a as color-coded dot curves for comparison. To estimate the flexural point F and hydrostatic point H from the elevation anomalies after cross-track slope correction, the Mean Absolute Elevation Anomaly (MAEA) (Figure 5c) was calculated from corrected elevation anomalies by averaging

135    the absolute values of each elevation anomaly profile shown in Figure 5b.

The flexural point F is the landward limit of ice flexure from tidal motion (Fricker and Padman 2006). The region where the MAEA is close to zero (the region to the left of point F in Figure 1) is regarded as the fully grounded ice. Based on this definition, the flexural point F is estimated to be the point where the gradient of the MAEA first increases from zero, and the second derivative of the MAEA reaches its positive peak (Figure 5c). The hydrostatic point H is the inshore limit of the

140    floating ice shelf that is in hydrostatic equilibrium (the region to the right of point H in Figure 1) (Fricker and Padman 2006). It is also where the elevation anomalies are consistent with the local tidal amplitudes and the MAEA reaches a maximum, becoming stable. The hydrostatic point H is then estimated to be the transition point where the gradient of the MAEA finally decreases to zero and the second derivative of the MAEA reaches its negative peak (Figure 5c). To reduce the influence of small-scale noise on the MAEA curve during the extraction of GZ features, a Butterworth low-pass filter with a normalized

145    cut-off frequency of 0.016 and an order of 5 was applied (Figure 5d). The low-pass filter removed the high-frequency noise without changing the shape of the MAEA curve therefore it won't influence the local transition points. A set of multiple peaks were then extracted from the second derivative of the filtered MAEA. Despite the low-pass filter, noise still existed especially in the areas with complex topography, resulted in multiple peaks not associated with the GZ features. In order to select the correct peaks corresponding to GZ features, we fitted an error function weighted by a Gaussian function with the

150    variance of 0.005 to the MAEA (Figure 5d). The transition point from this ideal sigmoid curve was used as a guide to select the correct peak and find the GZ features. This allows the process to be automated in comparison to ICESat-1.

To find the flexural point F, we used the closest positive peak (from the second derivative of filtered MAEA) to the peak from the third derivative of the error function curve. Unlike the abrupt change in the gradient of elevation anomaly at point F, the gradient often tends slowly to zero at point H (Figure 5a and 5b) (Brunt et al. 2010). Therefore using the same approach as F to find point H results in its location being slightly landward compared with the real GZ signal. Instead, we used the peak from the fourth derivative of the error function curve as the guide. This point is closer to the transition point where the MAEA gradient finally decreases to zero, and the closest negative peak of the second derivative of filtered MAEA was used as point H. Additionally, the tidal height predictions at 10 km offshore from the reference GL for each repeat track were calculated from the CATS2008 Tidal Model, which is an update to the model described by Padman et al. (2002). The tidal heights provide an independent check for the tide-induced surface elevation changes at point H.

## 3.2 Crossover analysis

Changes in ice shelf elevation due to tidal variation also can be calculated at the crossovers from ascending and descending tracks (Figure 4b). To calculate the elevation change at these crossovers, we first found the two closest observations using a KDTree within a 100 m searching radius from the ascending track and the descending track. We then extracted all the elevation measurements within a 100 m searching radius of these two closest data points from each ascending track and descending track. The crossover location was calculated by fitting latitude-longitude coordinates of all measurements from each ascending and descending track into two quadratic functions and calculating the intersection of these two functions. If the valid elevation measurements did not exist on both sides of the crossover within the 100 m searching distance, then the crossover was discarded (Brenner et al. 2007). The elevation at the crossover was estimated by linearly interpolating the elevations for each ascending and descending track. Similar to repeat track analysis, the elevation change at the crossover not only includes the ocean tidal signal, but also a temporal signal of elevation change. In this study, as we are only considering crossovers with a time difference less than 91 days to eliminate the influence of temporal elevation change, we removed the crossovers where the elevation exceeded 20 m. For crossovers on floating ice, if the time stamps of the ascending and descending tracks at the crossover are in the same phase of ocean tide cycle, the elevation change at this crossover should be close to zero, and it will be difficult to determine if the ice is floating or not. To eliminate these occurrences, the CATS2008 Tidal Model was used to calculate the tidal amplitude changes at each crossover and they were used as a reference for the vertical movements of floating ice. We extracted the minimum detectable tidal amplitude from the repeat track analysis to be 20 cm based on the results in section 4, and set the minimum threshold of the elevation change due to ocean tides on floating ice measured by the crossover analysis to be 40 cm. If both the modelled tidal amplitude and the elevation change at crossover are lower than this threshold, the ascending and descending tracks are likely to be in the same tidal phase and this crossover was discarded.

## 4 Results

Using the algorithm for GZ features estimation developed in this study, 69 flexural F points and 71 hydrostatic H points were estimated, their distributions are shown in Figure 6a and 6b along with the ICESat-1 GZ features (Brunt 2010) and the

185  DInSAR GL (Rignot 2016). The positions of ICESat-2 derived GZ features have better coverage compared with ICESat-1 GZ product which has 30 F points and 30 H points across the Larsen C Ice Shelf (Figure 6a and 6b). The improvement is especially notable in heavily crevassed regions like Jason Peninsula and Churchill Peninsula (Jansen et al. 2010), where 33 F points were obtained from ICESat-2 compared to 5 F points from ICESat-1.

The locations of the F point calculated from ICESat-2 data are in good agreement with the DInSAR GL (Rignot 2016) and

190  the ICESat-1 derived F point (Figure 6a). The mean absolute separation and standard deviation between the ICESat-2 F point and Rignot (2016) DInSAR GL are 0.29 km and 0.31 km, respectively. When comparing the ICESat-2 derived F point to ESA CCI DInSAR GL (ESA Antarctic Ice Sheet Climate Change Initiative, 2017), the mean absolute separation and standard deviation are 0.42 km and 0.38 km, respectively. Figure 6c shows the absolute separations between the DInSAR GL (Rignot 2016) and the point F estimated from ICESat-2 data. 78% of the F points are located less than 0.5 km away from the

195  DInSAR GL. In comparison, the standard deviations between CyroSat-2 derived GL and the DInSAR GL and ICESat-1 derived F point are 1.1 km and 1 km, respectively. The standard deviation between the ICESat-1 derived point F and the DInSAR GL is 0.9 km (Dawson and Bamber 2017). As the ICESat-1 derived H point is the only existing product we can compare for the H point in this study, we cannot directly quantify the separation and standard deviation between these two products due to the scarcity of ICESat-1 H point observations. However, the H point calculated in this study were validated

200  against the zero mean tidal amplitudes calculated from the CATS2008 tidal model as shown in track 1192 (Figure 5) and track 506 (Figure 7).

The largest deviation between the ICESat-2 derived point F and the DInSAR GL in Figure 6c is 2.51 km. This F point is located on Churchill Peninsula as shown in the black dashed box and the inset map in Figure 6a, and it was calculated from the repeat tracks of beam pair 1 of track 506 (Figure 7). The difference in position is not because of the incorrect

205  interpretation of point F but likely due to the existence of a lightly grounded ice plain. Between the ICESat-2 F point (vertical red dash line) and the reference GL (Depoorter et al. 2013) (vertical black dash line) in Figure 7a, the elevation anomalies of two left ground tracks 'c03_1l' (blue dash curve) and 'c04_1l' (orange dash curve) from cycles 3 and 4 always have similar values, while the elevation anomalies of two right ground tracks 'c03_1r' (red dash curve) and 'c04_1r' (green dash curve) are close to each other. The deviation of elevation anomalies between left ground tracks and right ground tracks

210  indicates the distributions of elevation anomalies in this region were caused by the cross-track slope between the left and right ground tracks, rather than the ocean tidal displacement. If the elevation changes are caused by ocean tides, the elevation anomalies of two repeat tracks from one repeat cycle such as tracks 'c03_1l' and 'c03_1r' with the same time stamp should be similar because the tide amplitudes are the same. This is confirmed by the near-zero elevation anomalies after the cross-

track slope correction in region between the vertical red dash line and the vertical black dash line in Figure 7b. Thus we
215  hypothesize that the GL identified by DInSAR in this region is actually the coupling line at the upstream edge of an ice plain
rather than the true GL (Brunt et al. 2010; Brunt et al. 2011).

Similar to repeat track analysis, the elevation changes at crossovers on floating ice caused by tidal movement will be high,
while they are close to zero on land ice where there is no vertical movement caused by ocean tides. Therefore, the elevation
change from the crossover analysis can provide additional information on the GL location. The distributions of the absolute
220  elevation changes |dh| at crossovers in Jason Peninsula and Churchill Peninsula are shown in Figure 8a and the crossovers in
Kenyon Peninsula are shown in Figure 8b. The overall distributions of |dh| align well with the point F derived from the
repeat track analysis, with low |dh| values on the landward region and high |dh| values on the seaward region of point F.
Figure 8c shows one set of crossovers with the same time difference from three beam pairs of the ascending track 1131 and
the descending track 1245 in repeat cycle 1. The F points (black dots) calculated from the repeat track analysis are located in
225  the middle between the high |dh| crossovers on floating ice and the low |dh| crossovers on land ice. This provides an
additional validation that the F points calculated from the repeat track analysis are accurate.

The GZ width depends on ice rheology, ice velocity, geometry of the GL and tidal range. The along-track distance between
points F and H calculated from the same track, however, can overestimate the actual GZ width as the orientation of ICESat-2
beam tracks are not always perpendicular to the GL. Besides, the intersection angle between the ICESat-2 ground track and
230  the GL varies. To calculate the GZ width at a perpendicular direction with the GL, we adopted a similar method used in
Brunt et al. (2010). By assuming that the reference GL used in section 3.1 provides a good reference for the local orientation
of the actual GL, we calculated the GZ width at each point F to be the length of the perpendicular line from point H to the
tangent line of the reference GL at the intersection between the nominal reference track and this reference GL. Width of 61
GZs were calculated in this study (Figure 6d), which varies from 0.29 km to 9.73 km with an average of 2.88 km, and the
235  standard deviation is 1.89 km.

## 5 Discussion

The ability of satellite laser altimetry data to estimate the Antarctic GL has been widely discussed in previous research using
ICESat-1 repeat track data (Brunt et al. 2010; Brunt et al. 2011; Fricker et al. 2009; Fricker and Padman 2006). The aim of
this study is to assess the capability and the accuracy of ICESat-2 laser altimetry data for estimating the GZ features of the
240  Antarctic Ice Sheet including flexural point F and hydrostatic point H. The new automated method presented in this study
should allow a more efficient and consistent mapping of the Antarctic GZ features. The combination of the flexural point F
and the hydrostatic point H can provide an important insight into the GZ structure such as the GZ width in Figure 6d, and the
ice dynamics inside the GZ which exceeds the research scope of this study.

To maximize the useable repeat tracks from the limited three repeat cycles released to date, the new method takes two
245   ground tracks of one beam pair from one repeat cycle as two repeat tracks. This enables the use of the internal cross-track
slope from one beam pair to eliminate the cross-track slope induced elevation change, which was a common problem when
using ICESat-1 data in the GZ estimation (Brunt et al. 2010) and improves the interpretation of GZ features. In addition, this
also allows us to calculate the GZ features from just two time stamps of tidal amplitudes, based on two out of three repeat
cycles spanning 8 months from March 29, 2019 to November 15, 2019 as shown in track 1192 (Figure 5) and track 506
250   (Figure 7). These two tracks only used data from two repeat cycles 3 and 4. It shows the potential of using the combinations
of different repeat cycles to estimate the GZ features repeatedly and continuously as more observations are acquired in the
future, making it possible to detect short-term GL changes caused by ocean tides and longer term GL retreat (Friedl et al.
2019). This represents a marked improvement compared with the ICESat-1 repeat track analysis which required multiple
repeat tracks (normally from at least five repeat cycles) with large temporal differences (Brunt et al. 2010; Brunt et al. 2011).
255   It also improves upon other non-altimetry approaches such as DInSAR, which was limited by the availability of suitable
short repeat pass SAR images (Rignot et al. 2011).

The small mean absolute separation of 0.29 km and standard deviation of 0.31 km between the ICESat-2 derived GL and the
DInSAR GL (Rignot 2016), show the improved precision of using ICESat-2 altimetry data in GL estimation compared with
other altimetry data such as ICESat-1 and CryoSat-2. With these methods, the deviation of GL from ICESat-1 repeat track
260   analysis with the DInSAR GL is ~0.9 km (Brunt et al. 2010), and the deviation between the CryoSat-2 GL and the DInSAR
GL is ~1.1 km (Dawson and Bamber 2017). In addition to an improved precision, our ICESat-2 derived GL has a better
coverage compared with ICESat-1, with more than 2 times higher density of both F point and H point on the Larsen C Ice
Shelf. In addition, the analysis of track 506 in Figure 7 shows the ability of using ICESat-2 repeat tracks to detect ice plains
that are difficult to capture from DInSAR or MODIS-based Mosaic of Antarctica (MOA) images (Brunt et al. 2011). Since
265   the GL can migrate by several kilometres with tides over ice plains, the ability to map them is a valuable feature of the
approach we have developed.

The lowest tidal amplitude can be detected by our method on the Larsen C Ice Shelf is 20 cm (Figure 7) and this is one of the
most northerly ice shelves with complex relief. By proving the approach works in this region of the ice sheet, it demonstrates
the ability for the generation of GLs for the majority of the Antarctic Ice Sheet, from regions with low tidal ranges such as
270   the Amundsen Bay Embayment (0.8 m - 1 m) to regions with large tidal range such as the Ross Ice Shelf (~1 m – 2 m) and
the Filchner-Ronne Ice Shelf (> 4m).

However, similar to previous studies on ICESat-1, several factors need to be considered when using the repeat track analysis
method for ICESat-2. The first is the surface roughness, as small scale topographic features such as crevasses can still
introduce residuals to the elevation anomaly. These features were not fully removed after applying the cross-track slope
275   correction, and can affect the final accuracy of the GZ features. Also, the forward scattering of cloud and blowing snow can

cause significant data loss for specific ground tracks, which is the case for Cole Peninsula and Northrop Peninsula as shown in Figure 2. The low densities of usable ground tracks in these two regions resulted in a lower coverage of GZ features (Figure 6).

280  The elevation changes of crossovers from the ascending and descending tracks also provide valuable information about the position of GL in the Antarctic Ice Sheet. Although the spatial separation between crossovers (Figure 8c) (~2 km) is far larger than the 20 m along-track separation of repeat track, it still can show the general location of the GL. It can also provide a validation for the GL position calculated from the repeat track analysis to check if it is reliable, especially in fast flowing ice streams where the GL often undergoes rapid changes (Rignot et al. 2011). Also, the study region Larsen C Ice Shelf is one of the northernmost ice shelves in Antarctica, subsequently being subject to the highest cross-track spacings.

285  With the cross-track spacing decreasing toward the southern region of the Antarctic Ice Sheet, higher density of crossovers will be available (e.g. ~ 6 per km$^2$ on the Ross Ice Shelf).

## 6 Conclusion

We have presented a new method to calculate the flexural point F and the hydrostatic point H of the GZ by determining the limits of tidal flexure using a repeat track analysis in combination with crossover analysis of ascending and descending

290  tracks from ICESat-2. This method addresses the issue of residuals in the elevation change caused by large cross-track slopes and enables an automated GZ estimation from a minimum of two repeat cycles. By using three repeat cycles during 8 month period between March 29, 2019 to November 15, 2019, we were able to calculate 69 flexural point F and 71 hydrostatic point H on the Larsen C Ice Shelf. It greatly improves the coverage of the GZ features compared with the ICESat-1 GL and shows the potential of a long time-series monitoring of the GL changes with more repeat cycles being released. The small

295  mean absolute separation 0.29 km and standard deviation of 0.31 km between the ICESat-2 derived GL and the DInSAR GL (Rignot 2016) show an improved precision of the GL estimation compared with the ICESat-1 and CryoSat-2 altimetry data. The lowest tidal range detected by this method on the Larsen C Ice Shelf is ~20 cm, making it possible to apply the repeat track analysis to other regions with low tidal range such as the Amundsen Sea Embayment. Although the distribution of elevation change from crossover analysis depends on the cross-track spacing of ICESat-2 ground tracks, it still shows a good

300  match with the GL calculated from the repeat track analysis. With smaller cross-track spacings in southern regions of the Antarctic Ice Sheet, the crossover analysis should provide better results regarding the GL location. The GZ mapping on the Larsen C Ice Shelf based on ICESat-2 data presented in this study shows an improved coverage and precision of GZ delineation and also indicates the ability for repeat observations of the GZ changes, this will significantly improve our understanding of the Antarctic GZ and its evolution in time with respect to climate and ocean forcing.

305

*Data availability.* The datasets generated in this study are available at doi TBC.

*Author contribution.* TL developed the methods and wrote the paper. GJD and SJC assisted with data processing. JLB conceived the study. GJD and JLB contributed to the interpretation of the results. All authors commented on the manuscript.

*Competing interests.* The authors declare no completing interest.

310 *Acknowledgments.* This work was supported by the China Scholarship Council (CSC) - University of Bristol joint-funded PhD Scholarship. The ICESat-2 data, DInSAR grounding line data and ICESat-1 grounding line data used in this study are available from the National Snow and Ice Data Center (NSIDC).

**References**

Arendt, A., Smith, B., Shean, D., Steiker, A., Petty, A., Perez, F., Henderson, S., Paolo, F., Nilsson, J., Becker, M.,
315 Adusumilli, S., Shapero, D., Wallin, B., Schweiger, A., Dickinson, S., Hoschuh, N., Siegfried, M., Neumann, T. (2019). ICESAT-2HackWeek/ICESat2_hackweek_tutorials, Version 1. Zenodo. http://doi.org/10.5281/zenodo.3360994

Brenner, A.C., DiMarzio, J.R., & Zwally, H.J. (2007). Precision and accuracy of satellite radar and laser altimeter data over the continental ice sheets. IEEE Transactions on Geoscience and Remote Sensing, 45, 321-331

Brunt, K.M., Fricker, H. A., Padman, L., and O'Neel, S. (2010). ICESat-Derived Grounding Zone for Antarctic Ice Shelves.
320 Boulder, CO: National Snow and Ice Data Center.

Brunt, K.M., Fricker, H.A., Padman, L., Scambos, T.A., & O'Neel, S. (2010). Mapping the grounding zone of the Ross Ice Shelf, Antarctica, using ICESat laser altimetry. Annals of Glaciology, 51, 71-79

Brunt, K.M., Fricker, H.A., & Padman, L. (2011). Analysis of ice plains of the Filchner–Ronne Ice Shelf, Antarctica, using ICESat laser altimetry. Journal of Glaciology, 57, 965-975

325 Christie, F.D.W., Bingham, R.G., Gourmelen, N., Tett, S.F.B., & Muto, A. (2016). Four-decade record of pervasive grounding line retreat along the Bellingshausen margin of West Antarctica. Geophysical Research Letters, 43, 5741-5749

Chuter, S., & Bamber, J. (2015). Antarctic ice shelf thickness from CryoSat-2 radar altimetry. Geophysical Research Letters, 42

Dawson, G., & Bamber, J. (2017). Antarctic Grounding Line Mapping From CryoSat-2 Radar Altimetry. Geophysical
330 Research Letters, 44

Depoorter, M., Bamber, J., Griggs, J., Lenaerts, J., Ligtenberg, S., van den Broeke, M., & Moholdt, G. (2013). Calving fluxes and basal melt rates of Antarctic ice shelves. Nature, 502, 89-92

ESA Antarctic Ice Sheet Climate Change Initiative (2017). Grounding line locations for the Ross and Byrd Glaciers, Antarctica, 2011-2017, Version 1. Center for Environmental Data Analysis.

335     Fricker, H.A., & Padman, L. (2006). Ice shelf grounding zone structure from ICESat laser altimetry. Geophysical Research Letters, 33

Fricker, H.A., Coleman, R., Padman, L., Scambos, T.A., Bohlander, J., & Brunt, K.M. (2009). Mapping the grounding zone of the Amery Ice Shelf, East Antarctica using InSAR, MODIS and ICESat. Antarctic Science, 21, 515-532

Friedl, P., Weiser, F., Fluhrer, A., & Braun, M.H. (2019). Remote sensing of glacier and ice sheet grounding lines: A review.
340     Earth-Science Reviews, 102948

Hogg, A.E., Shepherd, A., Gilbert, L., Muir, A., & Drinkwater, M.R. (2017). Mapping ice sheet grounding lines with CryoSat-2. Advances in Space Research, 62(6), 1191-1202

Howat, I.M., Porter, C., Smith, B.E., Noh, M.-J., & Morin, P. (2019). The reference elevation model of Antarctica. Cryosphere, 13, 665-674

345     Jansen, D., Kulessa, B., Sammonds, P., Luckman, A., King, E., & Glasser, N. (2010). Present stability of the Larsen C ice shelf, Antarctic Peninsula. Journal of Glaciology, 56, 593-600

Joughin, I., Smith, B.E., & Holland, D. (2010). Sensitivity of 21st century sea level to ocean-induced thinning of Pine Island Glacier, Antarctica. Geophysical Research Letters, 37

Konrad, H., Shepherd, A., Gilbert, L., Hogg, A.E., McMillan, M., Muir, A., & Slater, T. (2018). Net retreat of Antarctic
350     glacier grounding lines. Nature Geoscience, 11, 258

Le Meur, E., Sacchettini, M., Garambois, S., Berthier, E., Drouet, A., Durand, G., Young, D., Greenbaum, J., Holt, J., & Blankenship, D. (2014). Two independent methods for mapping the grounding line of an outlet glacier-an example from the Astrolabe Glacier, Terre Adélie, Antarctica. The Cryosphere, 8, 1331-1346

Markus, T., Neumann, T., Martino, A., Abdalati, W., Brunt, K., Csatho, B., Farrell, S., Fricker, H., Gardner, A., & Harding,
355     D. (2017). The Ice, Cloud, and land Elevation Satellite-2 (ICESat-2): Science requirements, concept, and implementation. Remote Sensing of Environment, 190, 260-273

Moholdt, G., Nuth, C., Hagen, J.O., & Kohler, J. (2010). Recent elevation changes of Svalbard glaciers derived from ICESat laser altimetry. Remote Sensing of Environment, 114, 2756-2767

Mouginot, J., B. Scheuchl, and E. Rignot (2017). MEaSUREs Antarctic Boundaries for IPY 2007-2009 from Satellite Radar,
360     Version 2. Boulder, CO: National Snow and Ice Data Center.

Neumann, T.A., Martino, A.J., Markus, T., Bae, S., Bock, M.R., Brenner, A.C., Brunt, K.M., Cavanaugh, J., Fernandes, S.T., & Hancock, D.W. (2019). The Ice, Cloud, and Land Elevation Satellite–2 mission: A global geolocated photon product derived from the Aadvanced Ttopographic Llaser Aaltimeter Ssystem. Remote Sensing of Environment, 233, 111325

Padman, L., Fricker, H.A., Coleman, R., Howard, S., & Erofeeva, L. (2002). A new tide model for the Antarctic ice shelves
365     and seas. Annals of Glaciology, Vol 34, 2002, 34, 247-254

Paolo, F.S., Fricker, H.A., & Padman, L. (2015). Volume loss from Antarctic ice shelves is accelerating. Science, 348, 327-331

Rignot, E., Mouginot, J., & Scheuchl, B. (2011). Antarctic grounding line mapping from differential satellite radar interferometry. Geophysical Research Letters, 38

370  Rignot, E., Mouginot, J., Morlighem, M., Seroussi, H., & Scheuchl, B. (2014). Widespread, rapid grounding line retreat of Pine Island, Thwaites, Smith, and Kohler glaciers, West Antarctica, from 1992 to 2011. Geophysical Research Letters, 41, 3502-3509

Rignot, E., J. Mouginot, and B. Scheuchl (2016). MEaSUREs Antarctic Grounding Line from Differential Satellite Radar Interferometry, Version 2. Boulder, CO: National Snow and Ice Data Center.

375  Rignot, E., J. Mouginot, and B. Scheuchl (2017). MEaSUREs InSAR-Based Antarctica Ice Velocity Map. Boulder, CO: National Snow and Ice Data Center.

Rignot, E., Mouginot, J., Scheuchl, B., van den Broeke, M., van Wessem, M.J., & Morlighem, M. (2019). Four decades of Antarctic Ice Sheet mass balance from 1979–2017. Proceedings of the National Academy of Sciences, 201812883

Schoof, C. (2007). Ice sheet grounding line dynamics: Steady states, stability, and hysteresis. Journal of Geophysical

380  Research: Earth Surface, 112

Smith, B., Fricker, H.A., Holschuh, N., Gardner, A.S., Adusumilli, S., Brunt, K.M., Csatho, B., Harbeck, K., Huth, A., & Neumann, T. (2019). Land ice height-retrieval algorithm for NASA's ICESat-2 photon-counting laser altimeter. Remote Sensing of Environment, 111352

385
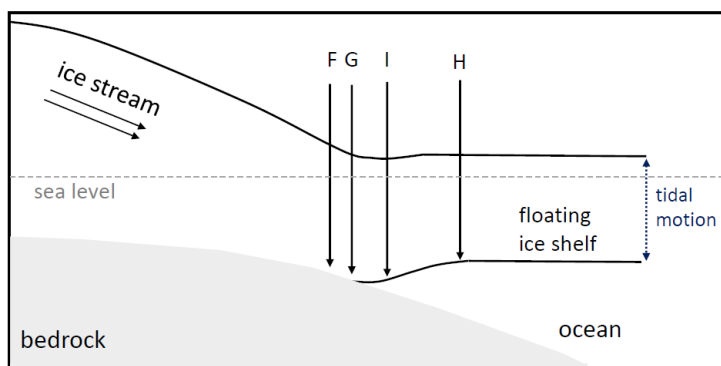
**Figure 1. Schematic of the ice shelf grounding zone structure adapted from Fricker and Padman (2006). Point G is the limit of ice flotation, point F is the landward limit of ice flexure induced by tidal motion, point H is the seaward limit of ice flexure and the inshore limit of hydrostatic equilibrium, point I is the break in surface slope.**
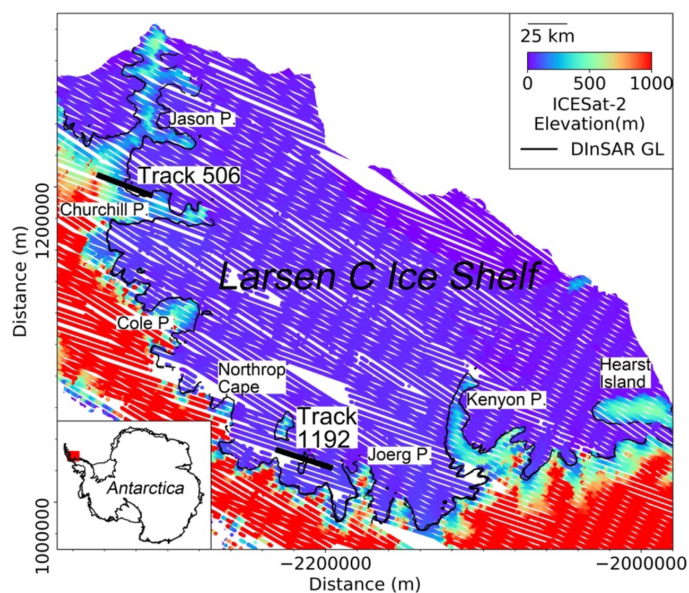
390

**Figure 2. Locations and surface elevations of ICESat-2 ground tracks from repeat cycles 3, 4 and 5 on the Larsen C Ice shelf. The black line is the GL calculated from DInSAR data (Rignot 2016). Red box on the inset map shows the location of the Larsen C Ice Shelf in Antarctica.**
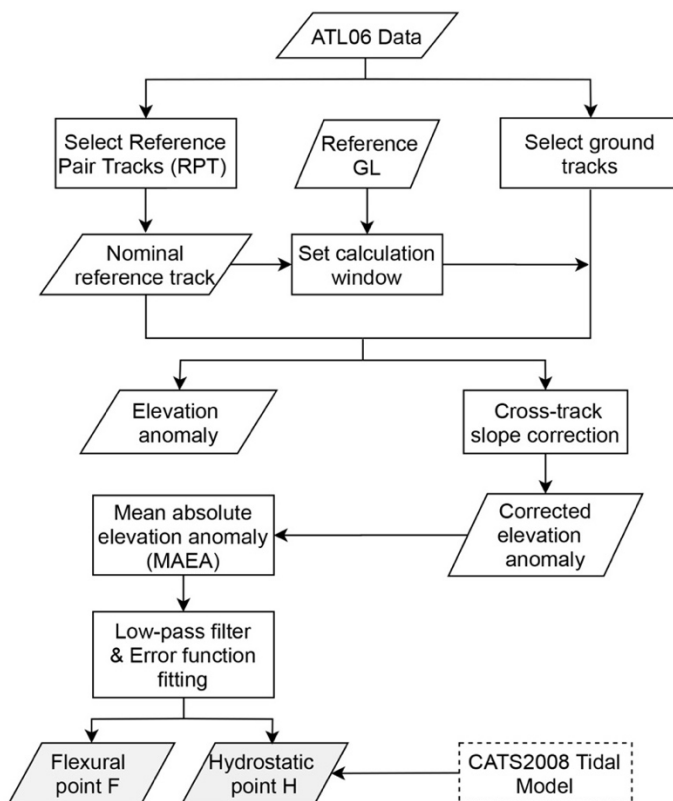
**Figure 3. Workflow of repeat track analysis in estimating the GZ features including point F and point H.**
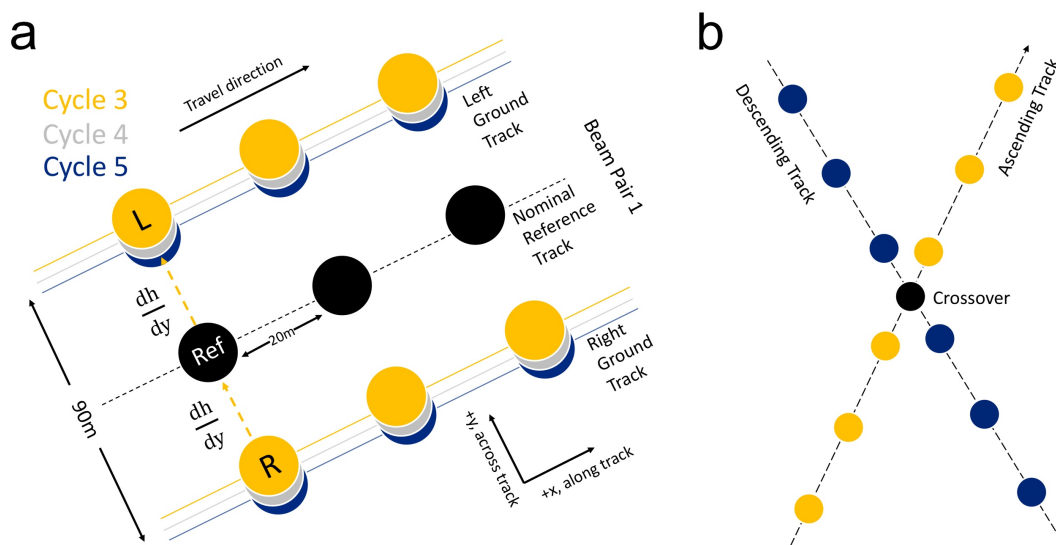
**Figure 4. a) Repeat track analysis method showing six repeat tracks from three repeat cycles 3, 4 and 5 for beam pair 1, including both left and right ground tracks in one beam pair from each repeat cycle. Black dots are the nominal reference track. Within**

each repeat cycle, elevations of both two ground tracks in a pair were corrected for cross-track slope onto the nominal reference
400    track. b) Crossover method showing the interpolation along the ascending track (yellow dots) and the descending track (blue dots)
to their intersection as the crossover (black dot).
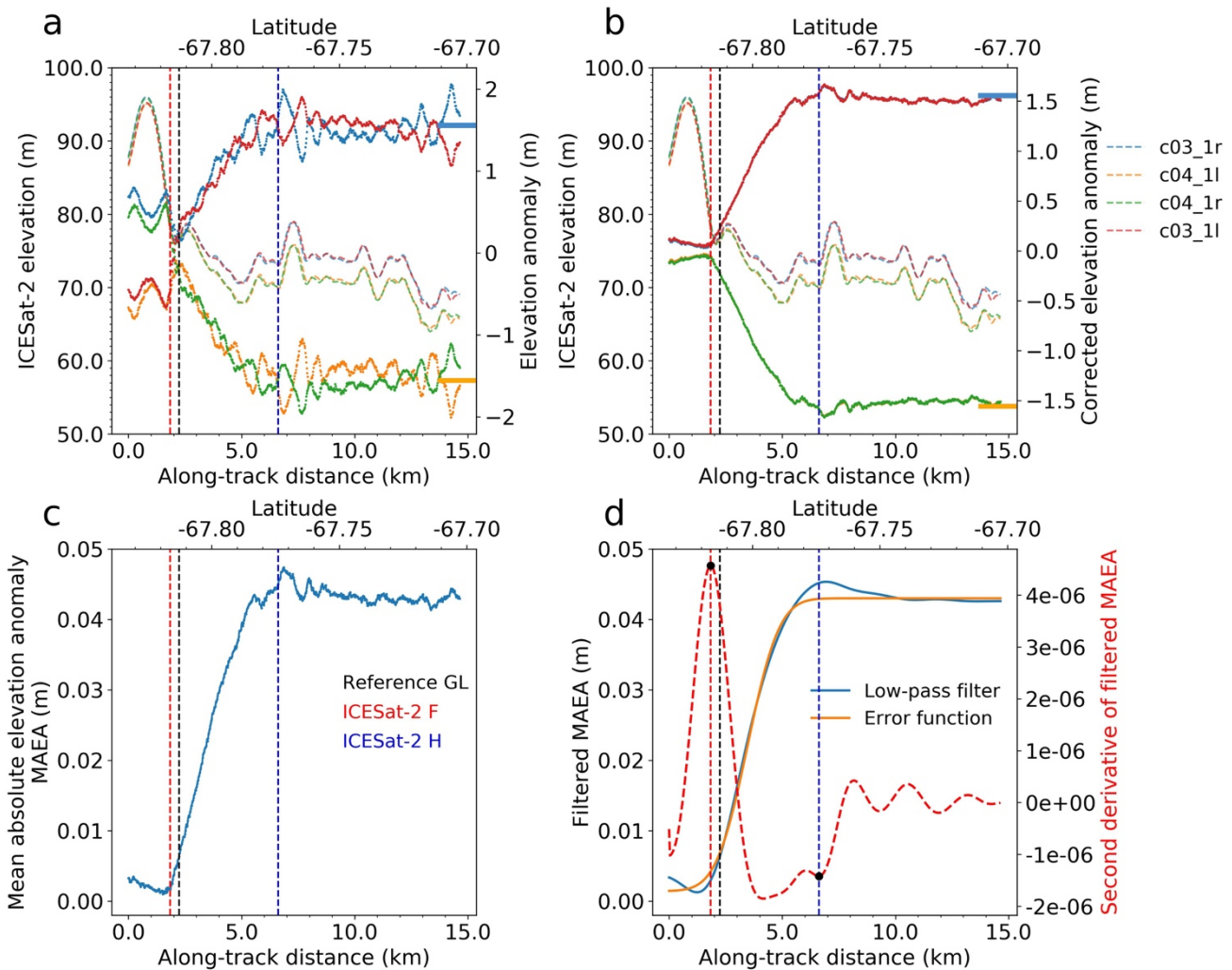
Figure 5. ICESat-2 repeat track analysis of beam pair 1 of track 1192 from repeat cycles 3 and 4, the location of the track 1192 is
405    shown in Figure 2. Each repeat track is denoted with the cycle number, beam pair number and the ground track location in right
('r') or left ('l'), e.g. 'c03_1r' is the right ground track in beam pair 1 from cycle 3. a) ICESat-2 're-tided' elevation profiles vs
along-track distance and latitude (transparent dashed curve in colours listed in the legend on the right). The elevation anomalies of
each track is colour-coded point line. b) ICESat-2 're-tided' elevation profiles and the corrected elevation anomalies after cross-
track slope correction. Horizontal lines at the right on Figures 5a and 5b are the zero mean tide height predictions from the
410    CATS2008 Tidal model (Padman et al. 2002). c) The Mean Absolute Elevation Anomaly (MAEA) by calculating the mean absolute
value of all corrected elevation anomalies shown in Figure 5b. d) Low-pass filter filtered MAEA is shown in blue line, error
function fitting of the MAEA is shown in yellow line, the second derivate of low-pass filter filtered MAEA is shown in red dashed
curve, the black dots are the locations of flexural point F (left) and hydrostatic point H (right). The location of point F is marked as
the vertical dashed red line in all subplots, the location of point H is marked as the vertical dashed blue line in all subplots, and the
415    location of reference GL from Mouginot (2017) is marked as the vertical dashed black line.
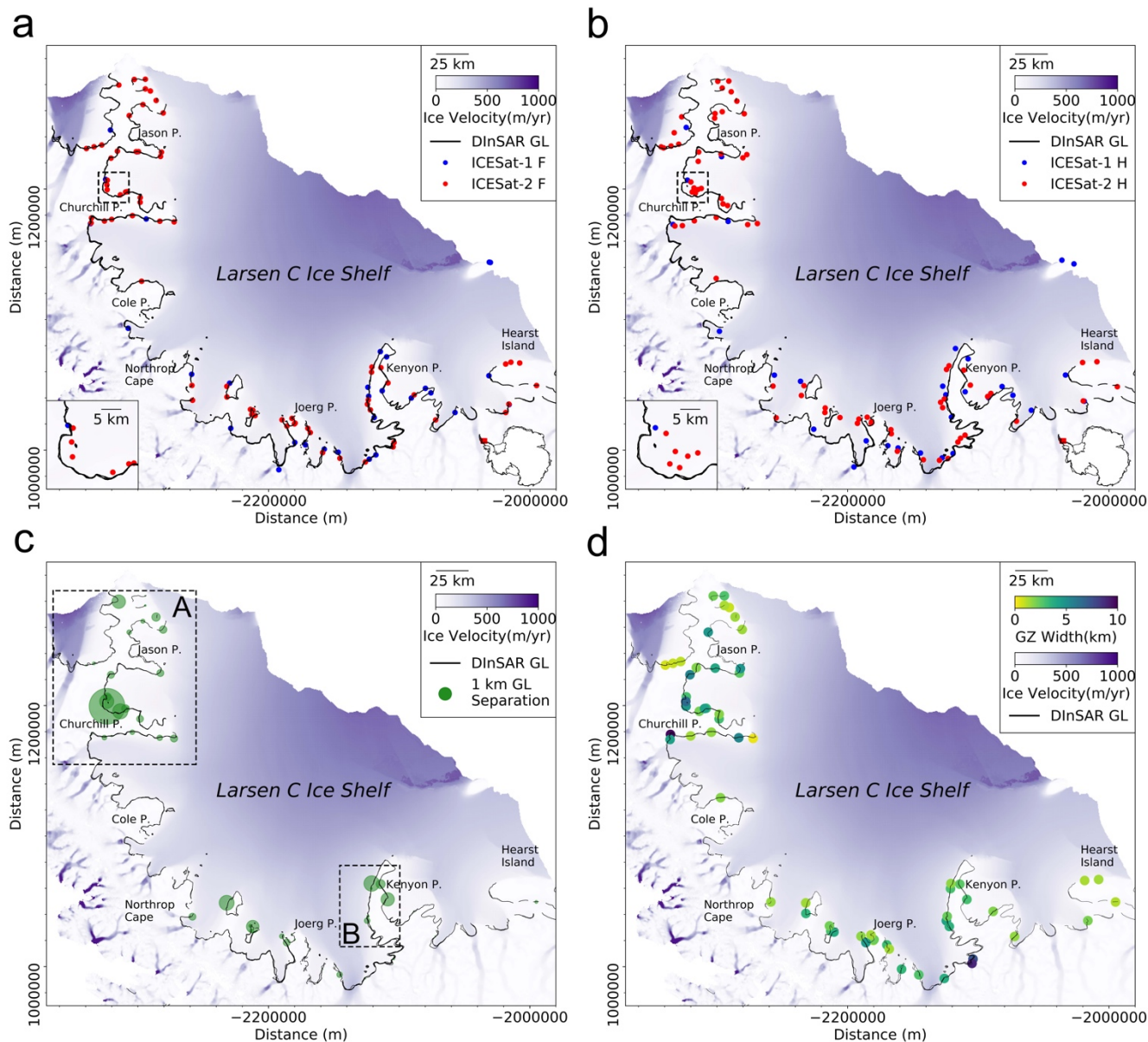
**Figure 6. a) Estimated locations of ICESat-2 derived flexural point F (red dots) overlain with ice velocity (Rignot 2017), the ICESat-1 derived flexural F points are shown in blue dots (Brunt 2010), DInSAR GL (Rignot 2016) is shown in black line. b) Estimated locations of ICESat-2 derived hydrostatic point H (red dots), the ICESat-1 derived hydrostatic H points are marked with blue dots (Brunt 2010) and the DInSAR GL (Rignot 2016) is shown in black line. The inset maps in Figures 6a and 6b are details of GZ features inside the black dashed box. c) The absolute separations between ICESat-2 derived flexural F points and DInSAR GL (Rignot 2016). d) The distribution of ICESat-2 derived GZ width in Larsen C Ice Shelf.**

420
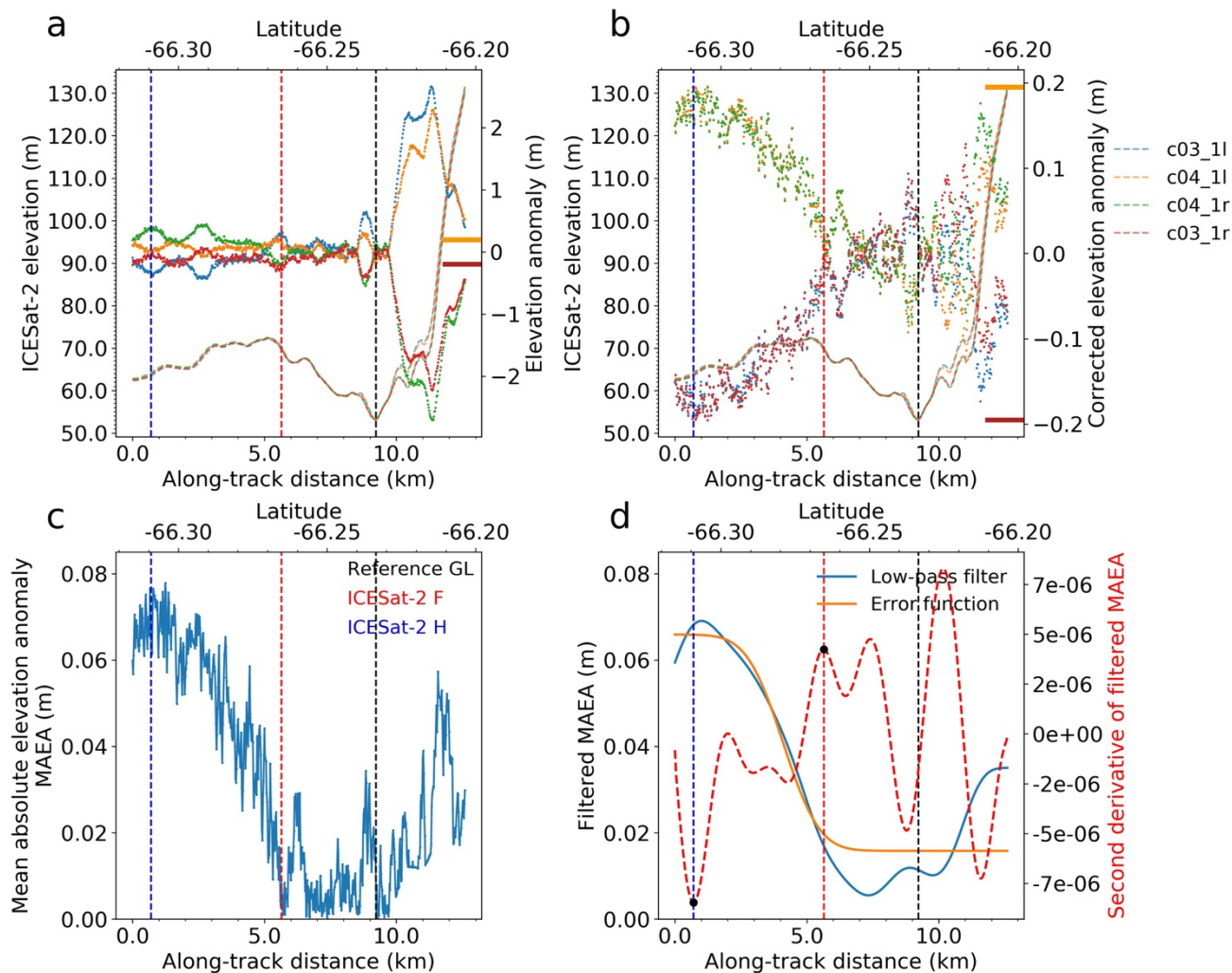
**Figure 7.** ICESat-2 repeat track analysis of beam pair 1 of track 506 from repeat cycles 3 and 4, the location of the track 506 is
shown in Figure 2. a) ICESat-2 'retided' elevation profiles vs along-track distance and latitude (transparent dashed curve in
colours listed in the legend on the right). The elevation anomalies of each track is colour-coded point line. b) ICESat-2 'retided'
elevation profiles and corrected elevation anomalies after cross-track slope correction. Horizontal lines at right on Figures 7a and
7b are the zero mean tide height predictions from the CATS2008 tidal model (Padman et al. 2002). c) The Mean Absolute
Elevation Anomaly (MAEA) by calculating the mean absolute value of all corrected elevation anomalies shown in Figure 7b. d)
Low-pass filter filtered MAEA is shown in blue line, error function fitting of MAEA is shown in yellow line, the second derivate of
low-pass filter filtered MAEA is shown in red dashed curve, the black dots are locations of flexural point F (left) and hydrostatic
point H (right). The location of point F is marked as the vertical dashed red line in all subplots, the location of point H is marked
as the vertical dashed blue line in all subplots, and the location of reference GL from Depoorter et al. (2013) is marked as the
vertical dashed black line.
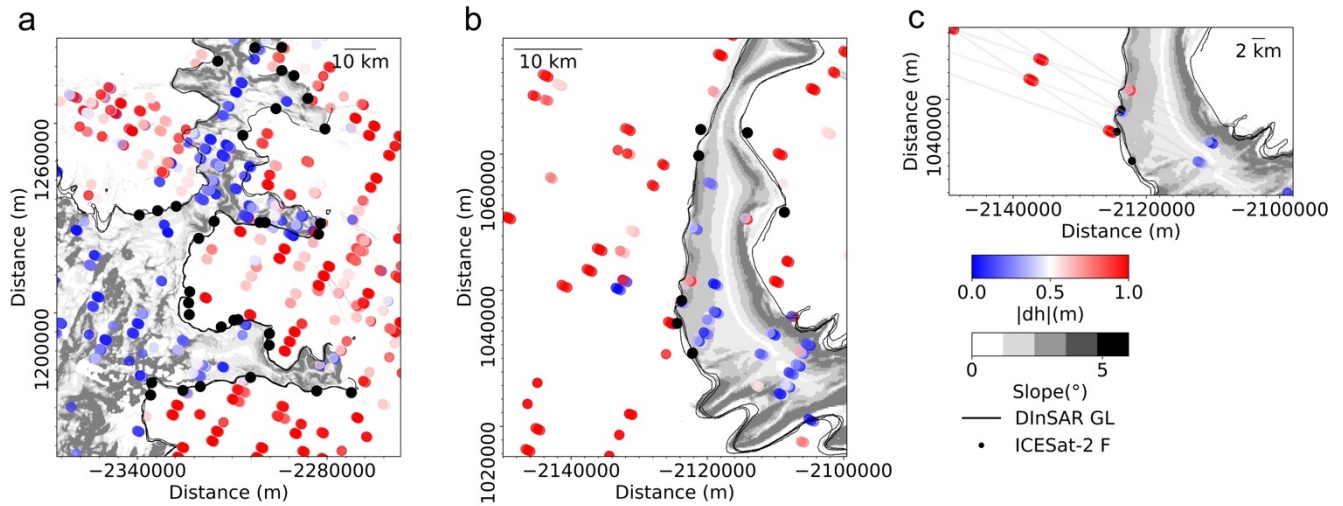
435

**Figure 8. Locations of the absolute elevations changes of the crossovers. a) Jason Peninsula and Churchill Peninsula shown in dashed black box A in Figure 6c. b) Kenyon Peninsula shown in dashed black box B in Figure 6c. c) A set of crossovers from three beam pairs of the ascending track 1131 and the descending track 1245 from repeat cycle 1. Background is the surface slope from the REMA DEM with a 250 m resolution (Howat et al. 2019).**

440

445